Journal of Materials Chemistry C

PAPER

Large negative magneto-LC effects induced by racemic dimerization of liquid crystalline nitroxide radicals with terminal cyano group

Received 00th January 20xx,
Accepted 00th January 20xx

DOI: 10.1039/x0xx00000x

www.rsc.org/

Takuya Akita, Daichi Kiyohara, Taira Yamazaki, Yoshiaki Uchida* and Norikazu Nishiyama

This article reports the synthesis and mesomorphism of new nitroxide radical compounds with a terminal cyano group and discusses the magneto-LC effects in the new compounds; one of the new compounds shows the largest decrease of paramagnetic susceptibility at the crystalline-to-liquid crystalline (LC) phase transition (negative magneto-LC effects) in the all-organic LC radicals reported thus far. The origins of the phenomenon are rationalized on the basis of the racemic magnetic dipolar interaction model using electron paramagnetic resonance (EPR) spectroscopy; the temperature dependences of Lorentzian and Gaussian components of line widths obtained by fitting EPR spectra with Voigt functions provide important insights.

Introduction

A lot of all-organic liquid crystalline (LC) radicals have been created thus far and their unique properties have been investigated. They are not only favourable from the point of view of the elements strategy in contrast to inorganic solid-state magnetic materials including heavy metal ions[1,2] but also promising multifunctional soft materials organized by the coupling between magnetism and the other properties based on the anisotropy of LC phases. Since the first example of paramagnetic LC radicals without metals was synthesized by Dvolaitzky *et al*. in 1974,[3] several types of all-organic calamitic,[4–18] bent-core[19,20] and discotic[21–24] LC radicals have been designed and synthesized.

LC nitroxide radicals (NRs) containing a five-membered ring NR moiety (PROXYL) in the mesogen core are one series of metal-free magnetic soft materials; they show thermally stable mesophases up to about 150 °C in the air,[9] there have been a lot of NRs showing a variety of LC phases such as nematic (N), smectic A (SmA) and smectic C (SmC) phases and the molecular chirality in the mesogen core induces chiral nematic (N*), chiral SmA (SmA*) and chiral SmC (SmC*) phases over a wide temperature range.[6–9,11–13,15–18] In addition, LC-NRs exhibit some fascinating properties in the externally applied fields;[9] *e.g.*, their droplets are attracted by a magnet,[25,26] which enables us to use LC-NRs as magnetically controllable carriers,[27] and SmC* LC-NRs confined in a thin LC cell show both ferroelectric and paramagnetic properties,[7] in which magnetic properties are controllable by applied electric fields through their molecular reorientation.[28] Furthermore, the decrease and increase of paramagnetic susceptibility occur at their crystalline (Cr)-to-LC phase transitions, which are called negative and positive magneto-LC effects, respectively.[9,11,12,16,25,26] For magnetic applications of LC-NRs, the mechanism of the magneto-LC effects has to be clarified.

The sign and magnitude of magneto-LC effects for the calamitic LC-NRs depend on the types of LC phases and molecular structures. As one of the symbolic examples, a racemate of LC-NR **1** with a terminal formyl group with a

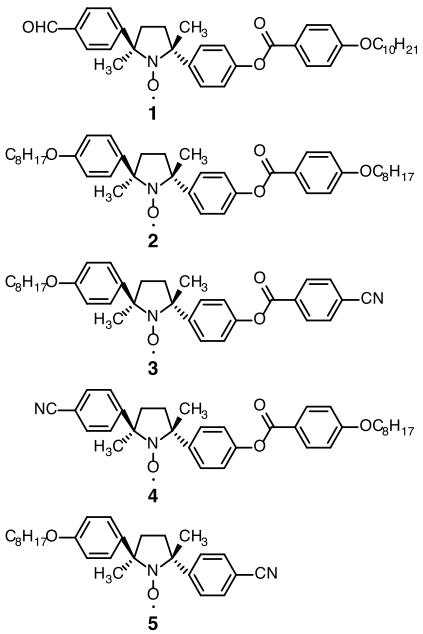

Fig. 1 Molecular structures of (2*R*,5*R*) enantiomers of compounds **1**–**5**.

Graduate School of Engineering Science, Osaka University, 1-3 Machikaneyama-cho, Toyonaka, Osaka 560-8531, Japan. E-mail: yuchida@cheng.es.osaka-u.ac.jp

† Electronic Supplementary Information (ESI) available: [details of any supplementary information available should be included here]. See DOI: 10.1039/x0xx00000x

positive dielectric anisotropy ($\Delta\varepsilon > 0$) shows weak negative magneto-LC effects, whereas both enantiomerically enriched **1** and racemate of LC-NR **2** with alkoxy side chains ($\Delta\varepsilon < 0$) instead of the terminal formyl group show the positive effects.[12,26] It indicates that the racemic antiferromagnetic dipolar interactions in N phase due to the strong interactions between electric dipoles ($\Delta\varepsilon > 0$) could be one of origins of the negative magneto-LC effects.[12] To examine whether the hypothesis is a universal tendency, the substitution of a cyano group for the terminal formyl group of the LC-NRs could be effective. This is because the compounds with a terminal cyano group are predicted to have a larger positive dielectric anisotropy than LC-NR **1** (5.4 Debye).[12] Moreover, the previously reported method to clarify the inhomogeneity of the intermolecular magnetic interactions[11] should be used for the LC-NRs with a positive dielectric anisotropy to rationalize the origin of the negative magneto-LC effects, too. Here, we report the synthesis and mesomorphism of NRs **3**–**5** with a terminal cyano group and discuss the magneto-LC effects in the new compounds on the basis of the racemic magnetic dipolar interaction model[12] using electron paramagnetic resonance (EPR) spectroscopy;[11,26] the temperature dependences of Lorentzian and Gaussian components of line widths obtained by fitting EPR spectra with Voigt functions elucidate the inhomogeneity of the intermolecular magnetic interactions.

Experimental

Instrumentation and Materials

Mass spectra were recorded on a JEOL JMS-700. IR spectra were recorded with a SHIMADZU IRAffinity-1. Elemental analyses (CHN) were obtained on a PerkinElmer 2400II. EPR spectra were recorded with a JEOL JES-FE1XG. Magnetization was recorded with a QUANTUM DESIGN MPMS-3. Phase transition behaviors were determined by differential scanning calorimetry (DSC) (SHIMADZU DSC-60), polarized optical microscopy (Olympus BX51) and X-ray diffraction (XRD) measurement. A hot stage (Japan High Tech 10083) was used as the temperature control unit for the microscopy. For variable temperature XRD measurement, the data collections were performed on a Rigaku RINT2200/PC-LH diffractometer using Cu-Kα radiation with 1.5418 Å. X-ray crystal structures were analyzed using a Rigaku Osmic VariMax diffractometer with graphite-monochromated Mo Kα radiation (λ = 0.71075 Å). Unless otherwise noted, solvents and reagents were reagent grade and used without further purification. Tetrahydrofuran (THF) that was used for the cyanation of aldehydes and EPR spectroscopy was distilled from sodium/benzophenone ketyl under nitrogen. The *g* values and hyperfine coupling constants (a_N) were determined by the EPR spectra of THF solutions at room temperature.

Chiral resolution of compound 6. A racemate of a phenolic NR compound **6** was prepared as a precursor according to the previously reported procedure.[17] The racemate of **6** was separated by using HPLC with a chiral column (DAICEL CHIRALCEL OD-H, 20 mm × 250 mm, particle size is 5 μm), hexane/2-propanol (9/1) as a mobile phase and flow rate of 20 mL/h in the similar way to the previously reported procedure.[17] The separated eluent was evaporated to obtain (2*S*,5*S*) and (2*R*,5*R*) enantiomers as more than 99% enantiomeric excess (*ee*).

Esterification to give compounds (±)-3 and (2*R*,5*R*)-3. The racemic and enantiomerically enriched (2*R*,5*R*) phenolic NR compounds **6** were esterified with 4-cyanobenzoic acid to afford the (±)-**3** and (2*R*,5*R*)-**3**. Dichloromethane (50 mL) was charged with **6** (0.12 g, 0.30 mmol), the 4-cyanobenzoic acid (0.044 g, 0.30 mmol), 1-(3-dimethylaminopropyl)-3-ethylcarbodiimide hydrochloride (EDC·HCl, 0.086 g, 0.45 mmol) and 4-(dimethylamino)pyridine (DMAP, 0.011 g, 0.09 mmol). After the mixture was stirred for 12 h at room temperature, the reaction solution was added saturated aqueous $NaHCO_3$ (50 mL), and extracted with diethyl ether (Et_2O, 50 mL × 2). The extract was dried over $MgSO_4$ and evaporated. The residue was purified by column chromatography on silica gel (hexane/ethyl acetate = 8/2 to 7/3) and recrystallized from hexane and Et_2O to afford the ester (±)-**3** and from hexane, Et_2O and CH_2Cl_2 to afford the optically active ester (2*R*,5*R*)-**3** as yellow crystals (50–60% yield).

Esterification to give compound (±)-8. A racemate of a phenolic NR compound **7** was prepared as a precursor according to the previously reported procedure.[12] To **7** (0.060 g, 0.19 mmol) dissolved in CH_2Cl_2 (5 mL) was added 4-octyloxybenzoic acid (0.056 g, 0.22 mmol), EDC·HCl (0.042 g, 0.22 mmol) and DMAP (0.0034 g, 0.028 mmol). After stirred overnight, the reaction mixture was poured into brine (20 mL), and the aqueous phase was extracted with Et_2O (30 mL × 3). The organic phase was washed with aqueous saturated $NaHCO_3$ solution and deionized water, and dried over $MgSO_4$ and concentrated in vacuo. Flash column chromatography on silica gel (hexane/CH_2Cl_2/Et_2O = 7/2/1) of the residue gave yellow solid **8** in 46% yield from **7**.

Cyanation to give compound (±)-4. To aldehyde **8** (0.049 g, 0.090 mmol) dissolved in tetrahydrofuran (THF, 7 mL) was added I_2 (0.050 g, 0.20 mmol) and 28wt% aqueous NH_3 solution (5 mL).[29] After the reaction mixture was stirred overnight at 50 °C, to it was added I_2 (0.053 g, 0.21 mmol) and 28wt% aqueous NH_3 solution (5 mL) additionally, and the mixture was stirred for 1 day. Then, 5wt% aqueous $Na_2S_2O_3$ solution (10 mL) was added to quench the reaction and the aqueous mixture was extracted with Et_2O (30 mL × 3), and the organic phase was dried over $MgSO_4$ and concentrated in vacuo. Flash column chromatography on silica gel (hexane/CH_2Cl_2/Et_2O = 5/4/1) of the residue gave yellow solid. The crude product was recrystallized from hexane/Et_2O (9/1) to give pure (±)-**4** in 10% yield from **8**.

Cyanation to give compound (±)-5. Racemate of a phenolic NR compound **9** was prepared as a precursor according to the previously reported procedure.[10] To aldehyde **9** (0.062 g, 0.15 mmol) dissolved in THF (2.5 mL) was added I_2 (0.041 g, 0.16 mmol) and 28wt% aqueous NH_3 solution (2.5 mL).[29] After the reaction mixture was stirred overnight at 50 °C, to it was added I_2 (0.042 g, 0.17 mmol) additionally, and the mixture was stirred for 1 day. Then, 5wt% aqueous $Na_2S_2O_3$ solution (10 mL) was added to quench the reaction and the aqueous mixture was extracted with Et_2O (30 mL × 3), and the organic phase was dried over $MgSO_4$ and concentrated in vacuo. Flash column chromatography on silica gel (hexane/CH_2Cl_2/Et_2O = 5/4/1) of the residue gave yellow solid. The crude product was recrystallized from hexane/Et_2O (9/1) to give pure (±)-**5** in 24% yield from **9**.

(±)-**3**: EPR (THF): g = 2.0058, a_N = 1.33 mT; IR (KBr) cm^{-1}: 2932, 2857, 2232, 1740, 1509, 1267, 1203, 1175, 1076, 762; HRMS (FAB+) m/z: $[M]^+$ calcd for $C_{34}H_{39}N_2O_4$ 539.2910; found 539.2914; Anal. Calcd for $C_{34}H_{39}N_2O_4$: C, 75.67; H, 7.28; N, 5.19. Found: C, 75.62; H, 7.31; N, 5.18.

(2*R*,5*R*)-**3**: EPR (THF): g = 2.0060, a_N = 1.34 mT; IR (KBr) cm^{-1}: 2928, 2855, 2234, 1746, 1508, 1273, 1250, 1177, 1078, 758; HRMS (FAB+) m/z: $[M]^+$ calcd for $C_{34}H_{39}N_2O_4$ 539.2910; found 539.2906; Anal. Calcd for $C_{34}H_{39}N_2O_4$: C, 75.67; H, 7.28; N, 5.19. Found: C, 75.76; H, 7.38; N, 5.22.

(±)-**4**: EPR (THF): g = 2.0061, a_N = 1.32 mT; IR (KBr) cm^{-1}: 2930, 2853, 2228, 1732, 1605, 1510, 1256, 1206, 1163, 1070, 843; HRMS (FAB+) m/z: $[M]^+$ calcd for $C_{34}H_{39}N_2O_4$ 539.2910; found 539.2906; Anal. Calcd for $C_{34}H_{39}N_2O_4$: C, 75.67; H, 7.28; N, 5.19. Found: C, 75.56; H, 7.37; N, 5.14.

(±)-**5**: EPR (THF): g = 2.0062, a_N = 1.33 mT; IR (KBr) cm^{-1}: 2930, 2866, 2228, 1607, 1508, 1242, 1184, 839; HRMS (FAB+) m/z: $[M]^+$ calcd for $C_{27}H_{35}N_2O_2$ 419.2699; found 419.2705; Anal. Calcd for $C_{27}H_{35}N_2O_2$: C, 77.29; H, 8.41; N, 6.68. Found: C, 77.27; H, 8.70; N, 6.67.

Determination of phase transition behaviors

The phase transition behaviors were characterized by DSC analyses, polarized optical microscopy and variable temperature XRD analyses. For DSC analyses, each powder sample of 2–3 mg was put into an aluminum sample pan. Each sample was heated and cooled at a rate of 2 °C/min under a flow of N_2 gas. For polarized optical microscopy, each sample was introduced by capillary action into an about 10-μm thick

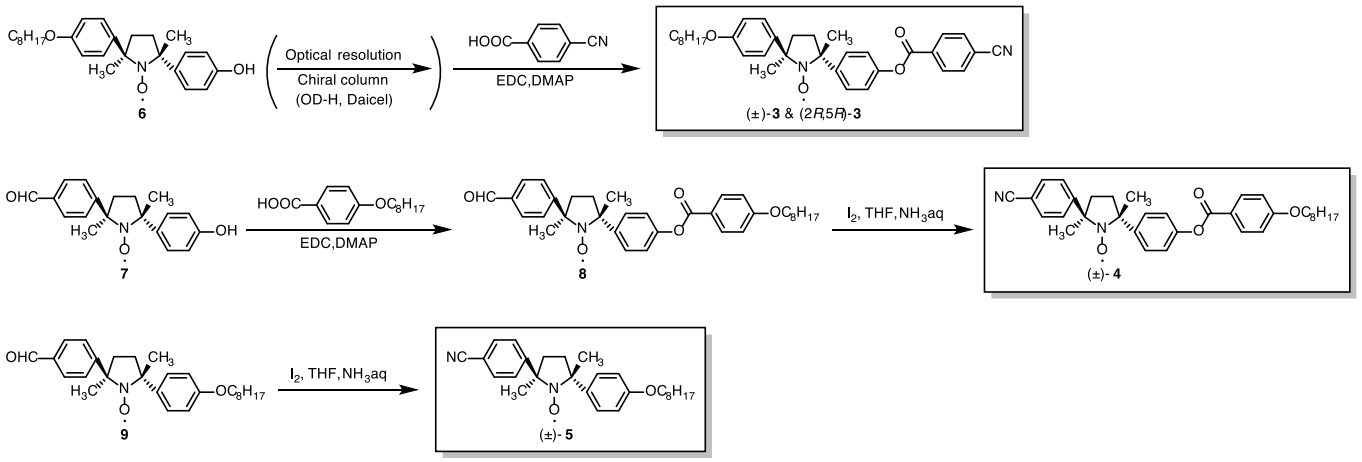

Scheme 1 Synthesis of **3**–**5**. Only (2*R*,5*R*) enantiomers are shown.

handmade glass sandwich cell in which the inner surfaces of the two glass substrates were treated with appropriate aligning agents. For XRD analyses, line profiles were recorded in the first heating processes.

Evaluation of magnetic properties by SQUID magnetometer

The temperature dependences of molar magnetic susceptibility were measured on a SQUID magnetometer in the first heating process. Each sample was enclosed in a DSC aluminum pan to prevent the sign inversion of the total magnetic susceptibility of samples in high temperature ranges. Curie constant and Weiss temperature were evaluated by fitting experimental magnetic susceptibility data with the Curie-Weiss law.

Derivation of relative paramagnetic susceptibility (χ_{rel}) from EPR spectra

The EPR spectra of **3** and **4** in the Cr, LC and isotropic (Iso) states in a magnetic field of about 0.33 T (X-band) by using a quartz tube (5 mm ϕ) were observed as shown in Fig. S1. Sweep time was 90 s, modulation width was 0.2 mT and time constant was 0.03 s. To discuss the weak effects by using accurately measured data, EPR spectra were measured in the narrow range of the magnetic field as shown in Fig. S2, and all spectra were almost Lorentzian first derivative curve in an ambient temperature range. To evaluate paramagnetic susceptibility from the EPR spectra by previously reported method,[26] we fitted the experimental data with the differential Lorentzian function

$$I'(H) = -16I'_{\mathrm{m}}\frac{H-H_0}{\Delta H_{\mathrm{pp}}/2}\left[3+\left(\frac{H-H_0}{\Delta H_{\mathrm{pp}}/2}\right)^2\right]^{-2}$$

where I'_{m} is the maximum peak height of the differential curve, H is the applied magnetic field, H_0 is the resonant magnetic field and ΔH_{pp} is the peak-to-peak line width. The experimental data can be well fitted with the above-mentioned differential Lorentzian function as shown in Fig. S3. By using the parameters directly obtained from the differential curves, such as I'_{m}, ΔH_{pp} and H_0, the paramagnetic susceptibility (χ_{para}) can be evaluated from Bloch equation as follows[11,26,30]

$$\chi_{\mathrm{para}} = \frac{2\mu_{\mathrm{B}} g I'_{\mathrm{m}} \Delta H_{\mathrm{pp}}^2}{\sqrt{3} h\nu H_1}$$

where μ_{B} is Bohr magneton, h is Planck's constant, v is the frequency of the absorbed electromagnetic wave, H_1 is the amplitude of the oscillating magnetic field, and g is the g-factor, which is inversely proportional to H_0. For plotting the temperature dependence of χ_{para}, the relative paramagnetic susceptibility (χ_{rel}), which is defined as

$$\chi_{\mathrm{rel}} = \frac{\chi_{\mathrm{para}}}{\chi_0}$$

where χ_0 is the standard paramagnetic susceptibility for each compound at 60 °C in the heating run, was used in place of χ_{para} to simplify the treatment. The magnetic data are the mean values of four measurements at each temperature to estimate χ_{para} with high accuracy.

Results and Discussion

Synthesis of compounds 3–5

Compounds **3**–**5** were prepared by the synthetic procedure shown in Scheme 1. According to the previously reported method,[18] compounds (±)-**3** and (2*R*,5*R*)-**3** were synthesized by the esterification of **6** with 4-cyanobenzoic acid. In the case of (2*R*,5*R*)-**3**, a phenolic precursor (±)-**6** was separated into enantiomerically enriched compounds by HPLC with a chiral column. The cyano groups of (±)-**4** and (±)-**5** were introduced at the final step through the cyanation of aldehydes. Aldehyde precursors (±)-**8** and (±)-**9** were prepared according to the previously reported methods including Grignard reactions and the deprotection of an acetal group.[10,12]

Effects of large dipole of cyano group on phase transition behaviors and molecular orientation

The phase transition behaviors of (±)-**3**, (2*R*,5*R*)-**3**, (±)-**4** and (±)-**5** were characterized by differential scanning calorimetry (DSC) at a scanning rate of 2 °C/min upon heating and cooling processes as shown in Fig. 2 and by polarized optical microscopy (POM) as shown in Fig. 3. DSC charts for (±)-**3**, (2*R*,5*R*)-**3** and (±)-**4** indicate that they show LC phases, whereas that for (±)-**5** indicates that it does not show any LC phase. XRD measurements for the LC phases give no peak (Fig. S4). Compounds (±)-**3** and (±)-**4** show thread-like and Schlieren textures typical of N phases in POM as shown in Fig. 3a and d, whereas (2*R*,5*R*)-**3** (>99% *ee*) exhibits an oily-streak texture characteristic of an N* phase (Fig. 3c).[31] Thus, the LC phases of (±)-**3**, (2*R*,5*R*)-**3** and (±)-**4** can be identified as an enantiotropic N phase, an enantiotropic N* phase, and an enantiotropic N phase, respectively. The effects of the cyano group on the stability of N phases are similar in both cases; whichever terminal alkoxy group of (±)-**2** is replaced with a cyano group, clearing points increase from 103.1 °C to 136.2 °C and 133.5 °C for (±)-**3** and (±)-**4**, respectively,[6] which is a well-known trend.[32] With regard to the crystallinity, they have small differences; supercooled N phase of (±)-**3** is crystallized at about 82 °C, whereas that of (±)-**4** is kept to lower than 60 °C, and (±)-**4** shows Cr-to-Cr phase transition at 108.0 °C in the heating process indicating a small enthalpy change. Furthermore, enantiomerically enriched (2*R*,5*R*)-**3** shows a lower melting point and a more stable LC phase than the racemate. In the cooling process, (2*R*,5*R*)-**3** shows the supercooled N* phase to about 78 °C. The about 20 °C drop of the melting point from racemates to the corresponding enantiomerically enriched samples commonly occurs for LC-NRs with a positive dielectric anisotropy ($\Delta\varepsilon > 0$).[12] In fact, the breaking of mirror symmetry in (2*R*,5*R*)-**3** destabilizes the molecular packing in the Cr phases, whereas the clearing points were not influenced. Meanwhile, LC-NRs **3** and **4** with a positive dielectric anisotropy show higher melting points than LC-NR **2** with negative dielectric anisotropy ($\Delta\varepsilon < 0$).[6] Furthermore, in the case of **2**, melting points of the racemate and enantiomerically enriched sample are almost the same. These results suggest that the existence of paired enantiomers with positive dielectric anisotropy ($\Delta\varepsilon > 0$) induces very dense molecular packing of LC-NRs. In addition, the absence of LC phases for (±)-**5** indicates that the rigid mesogen core with more than three benzene rings is needed to induce LC phases in the case of this type of LC-NRs.

Interestingly, in contrast to the previously reported LC-NRs without any polar terminal groups like (±)-**2**, which have difficulties to be aligned homeotropically (Fig. S5), the N phase of (±)-**3** exhibits a homeotropic alignment state in cells coated with several types of aligning agents. For example, (±)-**3** shows a uniform pseudo isotropic appearance in cells coated with well-known homeotropic aligning agents such as a polyimide JALS-204 (JSR Corp.) (Fig. 3b) and a cationic surfactant hexadecyltrimethylammonium bromide (C_{16}TAB) (Fig. S6a) indicating homeotropic alignment, whereas it shows Schlieren texture in a cell coated with an amorphous fluoropolymer CYTOP (Asahi Glass Co., Ltd.) (Fig. S6b) indicating planar alignment. The NR moiety could disturb the interactions between terminal side chains and aligning agents or could contact with the surfaces prior to side chains. Meanwhile, the SmA* phase of an analogue of (2*S*,5*S*)-**1** shows homeotropic alignment state.[12] These suggest that the terminal cyano group should stabilize homeotropic alignment state by contacting with aligning agents due to the dipole moment larger than the NR moiety.

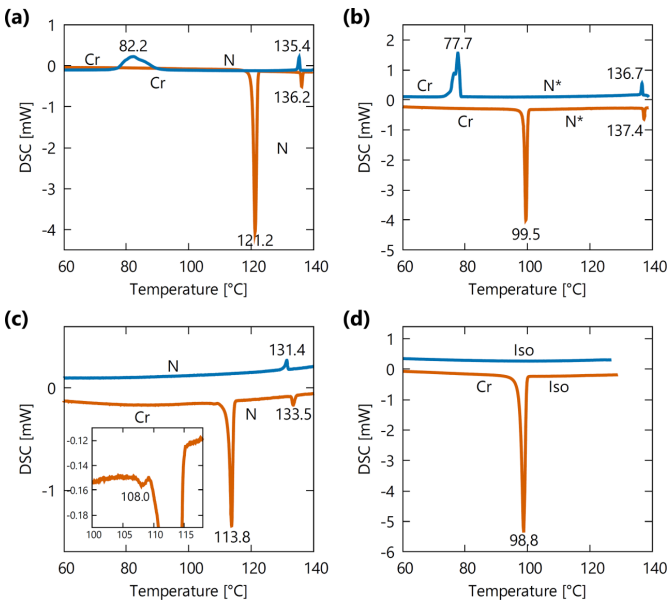

Fig. 2 DSC curves for (a) (±)-**3**, (b) (2*R*,5*R*)-**3**, (c) (±)-**4** and (d) (±)-**5**. Red and blue lines correspond to the heating and cooling processes, respectively. Transition temperatures are shown with standard notation of the phases: crystalline (Cr), nematic (N), chiral nematic (N*) and isotropic (Iso) phases.

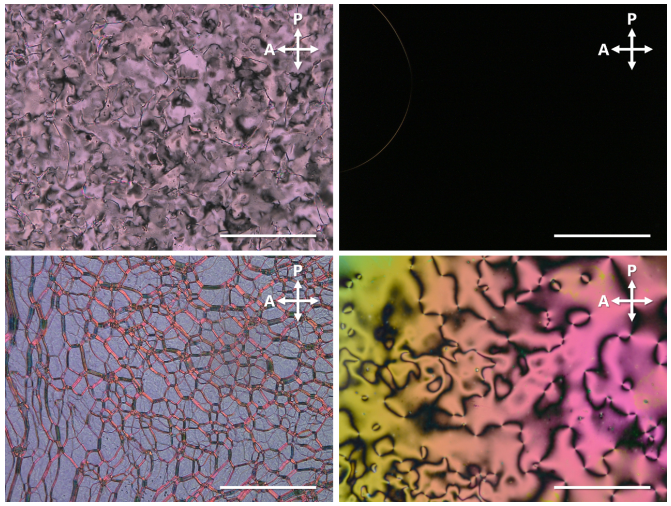

Fig. 3 Polarized optical micrographs of (±)-**3**, (2*R*,5*R*)-**3**, (±)-**4**. (a) A thread-like texture for the N phase at 125 °C of (±)-**3**. (b) A pseudo isotropic appearance for the N phase at 125 °C for (±)-**3** in a cell coated with polyimide JALS-204. The top-left corner in the image contains no sample. (c) An oily-streaks texture for the N* phase at 110 °C for (2*R*,5*R*)-**3**. (d) A Schlieren texture for the N phase at 120 °C for (±)-**4**. The orientations of polarizer (P) and analyzer (A) are shown. Scale bars correspond to 200 μm.

Temperature dependence of magnetic susceptibility in low temperature crystalline phases

To confirm that the magnetic interactions in the Cr phases, we measured molar magnetic susceptibility χ_M for the above four samples (±)-**3**, (2*R*,5*R*)-**3**, (±)-**4** and (±)-**5** on a SQUID magnetometer at a magnetic field of 0.5 T in the temperature range of 2–200 K in the first heating process. The magnetic properties of these compounds are summarized in Table 1. Here we define the sum of paramagnetic susceptibility χ_{para} and diamagnetic susceptibility χ_{dia} as the molar magnetic susceptibility ($\chi_M = \chi_{para} + \chi_{dia}$). The $\chi_{para}T$-T plots obeyed the Curie-Weiss law in the temperature range between about 100 and 200 K ($\chi_M = C/(T - \vartheta) + \chi_{dia}$: $C \sim 0.375$) (Fig. 4). These results indicate that the NR moieties are chemically stable, and all crystals of compounds **3**–**5** show weak intermolecular antiferromagnetic interactions at low temperature ($\vartheta < 0$).

The temperature dependences of $\chi_{para}T$ for (±)-**3**, (2*R*,5*R*)-**3**, (±)-**4** and (±)-**5** can be best fitted with the following Bleaney-Bowers equation for the singlet-triplet model of $S = 1/2$ with $\alpha > 0.94$ (Table 1 and Fig. 4),[33]

$$\chi_{\mathrm{para}}T = \frac{\alpha N g^2 \mu_B^2}{k_{\mathrm{B}}} \frac{1}{3 + \exp(-2J/k_{\mathrm{B}}T)}$$

where α denotes the radical purity of the sample, N is Avogadro constant, g is g-value, μ_B is Bohr magneton and k_B is Boltzmann constant. Singlet-triplet energy gaps J are summarized in Table 1. As mentioned above, all crystals of compounds **3**–**5** show antiferromagnetic interactions at low temperature, and (2*R*,5*R*)-**3** shows the largest interactions. To gain further insights into the observed antiferromagnetic interactions, we need to know the crystal structures of the compounds. Although, generally speaking, it is quite difficult to obtain large single crystals of LC compounds enough to decide the crystal structures because most of LC compounds show low-crystallinity due to their low symmetry and flexible side chains, we could fortunately obtain a single crystal of (±)-**3** from hexane and Et_2O and it gave us the crystal structure (Fig. S7, ESI), representing racemic dimer structure. The DFT calculations for the energy difference between the singlet and triplet states ($\Delta E = E_{singlet} - E_{triplet} = 2J$ for the dimer model) were performed on the racemic dimeric coordinate of (±)-**3** extracted from their 1D chain structure (Fig. S7b) using Gaussian 09 program package,[34] giving a singlet-triplet energy gap J/k_B value of –0.399 K for UBLYP/6-311G level, which are consistent with the experimental value of –0.445 K.[35,36] Therefore, we can conclude that the intermolecular interactions between NO groups in this geometry are responsible for the observed antiferromagnetic interactions. However, the direct O1···O5 contact (6.19 Å) may be too distant to be a source of the observed antiferromagnetic interactions (Fig. S7b). Therefore, the intermolecular exchange interactions between the NO group and the closest hydrogen and carbon atoms on *meta* position of the adjacent molecule could be responsible for the observed antiferromagnetic interactions (N1-O1···H51-C51 distance 2.56 Å and N3-O5···H11-C11 distance 2.70 Å). Then, we have actually computed the spin densities for the singlet state of the dimer. Spin density values are summarized in Table S1; the spin density values on these atoms on adjacent molecules have the opposite sign. Although there are a lot of covalent bonds between the NO group and the C11 and C51 atoms, these carbon atoms have enough spin density values resulted from the spin polarization to strongly interact with the NO group of the adjacent molecule. Because of very weak spin polarization in H11 and H51, the intermolecular antiferromagnetic exchange interactions through N1-O1···C51 (3.19 Å) and N3-O5···C11 (3.40 Å) would stabilize the singlet state of two adjacent molecules. Therefore, this intermolecular spin polarization exchange couplings through C11 and C51 atoms could contribute to observed bulk antiferromagnetic interactions of (±)-**3** in low temperature range.

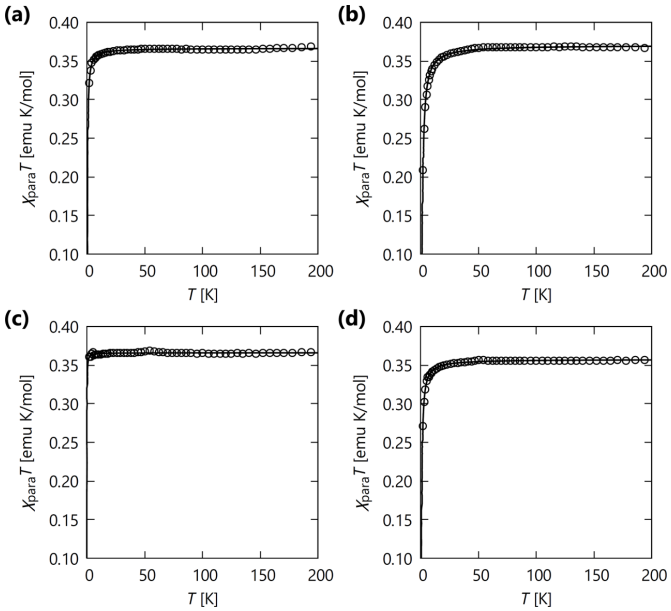

Fig. 4 $\chi_{para}T$-T plots of (a) (±)-**3**, (b) (2*R*,5*R*)-**3**, (c) (±)-**4** and (d) (±)-**5** at a field of 0.5 T in the heating process. Open circles represent the experimental data and solid lines show theoretical curve of Bleaney-Bowers equation for the singlet-triplet model.

Table 1 Magnetic properties of compounds.

Compound	C [a] [emu K mol^{-1}]	ϑ [b] [K]	J/k_B [c] [K]
(±)-**3**	0.367	−0.313	−0.445
(2*R*,5*R*)-**3**	0.369	−0.720	−1.446
(±)-**4**	0.366	−0.020	−0.063
(±)-**5**	0.357	−0.365	−0.808

[a]Curie constant. [b]Weiss temperature. [c]Singlet-triplet energy gap.

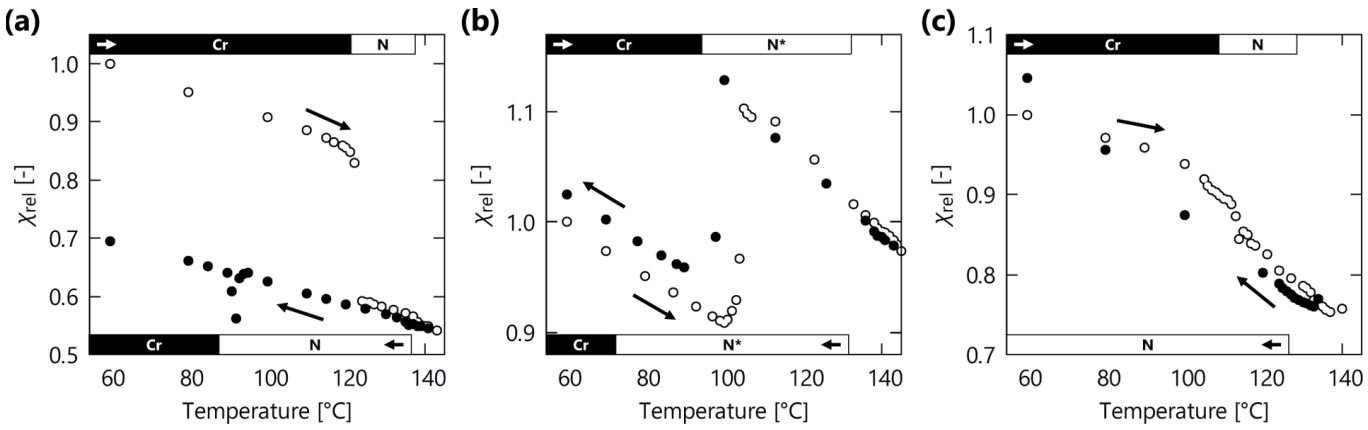

Fig. 5 Temperature dependences of χ_{rel} values for (a) (±)-**3**, (b) (2*R*,5*R*)-**3** and (c) (±)-**4**. Open and filled circles represent the first heating and cooling processes, respectively. Error bars are not shown because they are sufficiently small. The phase ranges determined by DSC analyses and *g*-value changes are shown in the upper and lower sides for heating and cooling processes, respectively.

Temperature dependence of magnetic susceptibility in high temperature LC phases

To study the difference between the magnetic behaviors in the solid and LC phases, we discuss the temperature dependences of paramagnetic susceptibility of (±)-**3**, (2*R*,5*R*)-**3**, (±)-**4** between 60 and 140 °C calculated from EPR spectroscopy (see Experimental section). The temperature dependences of relative paramagnetic susceptibility (χ_{rel}) are shown in Fig. 5. Both (±)-**3** and (±)-**4** show the same trends; the χ_{rel} values decrease (negative magneto-LC effects) at the Cr-to-N phase transitions in the heating process. In particular, (±)-**3** exhibited a large χ_{rel} decrease by 31% at the Cr-to-N phase transition (121 °C) in the heating process (Fig. 5a). Meanwhile, (±)-**4** showed a small χ_{rel} decrease at the Cr-to-N phase transition (114 °C) in the heating process (Fig. 5c). These results indicate that regardless of the position, the terminal substitution of a polar group like formyl and cyano groups induces negative magneto-LC effects for racemates.

The temperature dependence of χ_{rel} values for (2*R*,5*R*)-**3** shows positive magneto-LC effects. In contrast to the negative magneto-LC effects of (±)-**3**, (2*R*,5*R*)-**3** showed a distinct χ_{rel} increase by 21% at the Cr-to-N* transition (100 °C) in the heating process (Fig. 5b). These behaviours are likely to be consistent with the data from SQUID magnetometry (Fig. S8); however, since the scatter of the χ_M values at higher temperatures is too large and they contain temperature-dependent χ_{dia} values,[37] we cannot discuss the details of the magnetic behaviors using a SQUID magnetometer for LC-NRs.[12,26]

To gain an insight into the origin of negative and positive magneto-LC effects operating in the N and N* phase of (±)-**3** and (2*R*,5*R*)-**3**, respectively, the temperature dependence of ΔH_{pp} should be discussed with that of the χ_{rel} (Fig. 6). Generally, the change in ΔH_{pp} reflects the following two magnetic interactions: (a) spin–spin dipolar interactions (the stronger the interaction is, the more the ΔH_{pp} increases) and (b) spin–spin exchange interactions (the stronger the interaction is, the more the ΔH_{pp} decreases).[12,26]

In the case of (±)-**3**, an abrupt decrease in ΔH_{pp} occurred in concert with the abrupt decrease in χ_{rel} at the Cr-to-N phase transition (121 °C) in the heating run, indicating the increase of spin–spin exchange interactions in the N phase. It is thus likely that the negative magneto-LC effects in the N phase of (±)-**3** originate from the generation of antiferromagnetic spin-spin exchange interactions due to the local SOMO–SOMO overlapping in the dense packing of racemic dimers.[12] The formation of racemic dimers is supported by the phase transition behaviors; (±)-**3** shows higher melting point than (2*R*,5*R*)-**3** because the racemic dimerization renders the denser molecular packing.[17] In contrast to the racemate, (2*R*,5*R*)-**3** shows that an abrupt increase in ΔH_{pp} occurred in concert with the abrupt increase in χ_{rel} at the Cr-to-N* phase transition (100 °C) in the heating run, indicating the increase of spin–spin dipolar interactions in the N* phase. It is thus likely that the positive magneto-LC effects operating in the N* phase of (2*R*,5*R*)-**3** should originate from the generation of ferromagnetic spin–spin dipolar interactions and the absence of antiferromagnetic exchange interactions observed in racemic dimers.

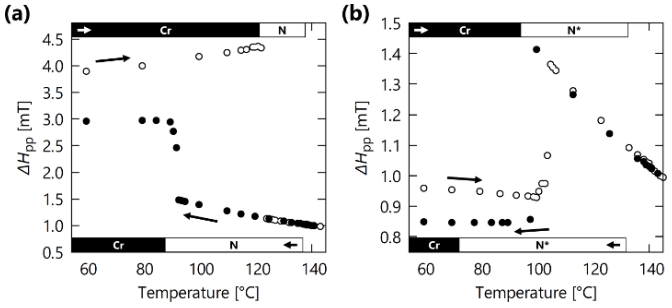

Fig. 6 Temperature dependence of ΔH_{pp} for (a) (±)-**3** and (b) (2*R*,5*R*)-**3** by EPR spectroscopy around a field of 0.33 T. Open and filled circles represent the first heating and cooling processes, respectively. Error bars are not shown because they are sufficiently small. The phase ranges determined by DSC analyses and *g*-value changes are shown in the upper and lower sides for heating and cooling processes, respectively.

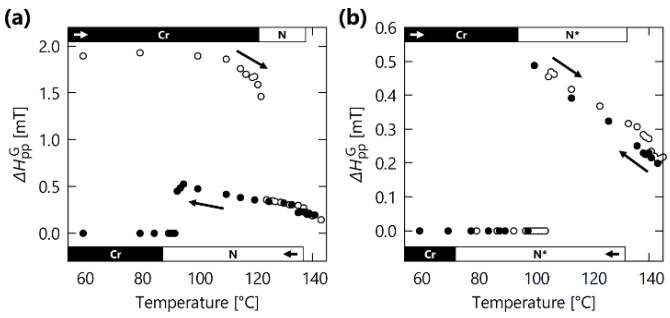

Fig. 7 Temperature dependence of $\Delta H_{pp}{}^{G}$ for (a) (±)-**3** and (b) (2*R*,5*R*)-**3** by EPR spectroscopy around a field of 0.33 T. Open and filled circles represent the first heating and cooling processes, respectively. Error bars are not shown because they are sufficiently small. The phase ranges determined by DSC analyses and *g*-value changes are shown in the upper and lower sides for heating and cooling processes, respectively.

Furthermore, the Gaussian component of EPR peak-to-peak line width ($\Delta H_{pp}{}^{G}$) reflects the inhomogeneous broadening of the EPR spectra, which is useful to discuss the influence of the inhomogeneous intermolecular contacts on the magneto-LC effects.[11] Although we fitted the observed EPR spectra with Lorentzian first derivative curve, it is well-known that EPR spectra are inhomogeneously broadened by the unresolved proton hyperfine coupling and magnetic-field modulation, and hence, the spectra become Voigt function, which is the convolution of Gaussian and Lorentzian functions.[38] The $\Delta H_{pp}{}^{G}$ contains the contribution of Gaussian line width in the limit of the zero modulation ($\Delta H_{pp0}{}^{G}$) and magnetic field modulation (κH_m), where H_m is the modulation amplitude and κ is a constant.[38] In our case, the contribution of inhomogeneous intermolecular contacts (H_{IIC}) should be added to the Gaussian component. Therefore, $\Delta H_{pp}{}^{G}$ can be expressed as the root-mean-square of the components.[11,38]

$$\Delta H_{pp}^{G\,2} = \Delta H_{pp0}^{G\,2} + \kappa^2 H_m^{\,2} + H_{IIC}^{\,2}$$

Among the terms, only $H_{IIC}{}^2$ depends on temperature. Thus, we can discuss the influence of inhomogeneous intermolecular contacts on the magneto-LC effects by analysing the temperature dependence of $\Delta H_{pp}{}^{G}$. Then, we fitted the spectra obtained from the numerical integration of the raw data $I(H)$ with the Voigt function to estimate $\Delta H_{pp}{}^{G}$

$$I(H) = I_V \int \frac{\exp\left[-2(H'-H_0)^2/\Delta H_{pp}^{G\,2}\right]}{1+\left(\frac{H'-H}{\sqrt{3}\Delta H_{pp}^{L}/2}\right)^2} dH'$$

where I_V is a constant, and $\Delta H_{pp}{}^{L}$ is the Lorentzian peak-to-peak line width influenced by the magnitude of intermolecular magnetic interactions. The numerical integration of the experimental data $I(H)$ can be well fitted with the above-mentioned Voigt function as shown in Fig. S9, and the parameter $\Delta H_{pp}{}^{G}$ was obtained as shown in Fig. 7.

We estimate the contribution of the inhomogeneity to the intermolecular magnetic interactions from the temperature dependence of $\Delta H_{pp}{}^{G}$. In the heating run, $\Delta H_{pp}{}^{G}$ decreases at the melting point for (±)-**3**, whereas $\Delta H_{pp}{}^{G}$ is quite small in the initial Cr phase, increases abruptly at the melting point, and then decreases with increasing temperature for (2*R*,5*R*)-**3**. The increase in $\Delta H_{pp}{}^{G}$ in the heating run indicates the appearance of inhomogeneous intermolecular magnetic interactions. These behaviors indicate that the decrease in inhomogeneous intermolecular contacts renders the magneto-LC effects negative, whereas the increase in inhomogeneous intermolecular contacts renders the magneto-LC effects positive. The more inhomogeneous the intermolecular magnetic interactions become, the more the average ferromagnetic interactions could increase. This is because the sign of intermolecular effective exchange integrals notably depends on the orientations and conformations of molecules.[39] As mentioned above, both (±)-**3** and (2*R*,5*R*)-**3** show weak intermolecular antiferromagnetic interactions in Cr phases at low temperature ($\vartheta < 0$), which suggests that the manner of intermolecular antiferromagnetic interactions occur easily. If the intermolecular interactions are sufficiently inhomogeneous, a certain amount of intermolecular ferromagnetic interactions, which hardly occur in homogeneous Cr phases, will occur frequently. Therefore, (2*R*,5*R*)-**3** shows the positive magneto-LC effects.

The terminal cyano group induced the hitherto largest negative magneto-LC effects (31% decrease) for (±)-**3**. Compound **3** has a strong electric dipole parallel to the molecular long axis, which is calculated as 7.1 Debye by DFT calculations at UBLYP/6-311G level using Gaussian 09 program package.[34] To minimize the electric dipolar interaction energies, the molecules will be required to pack in a head-to-tail arrangement like 4-pentyloxy-4'-cyanobiphenyl,[32] which can stabilize LC phases. The 20–30 °C higher clearing points of **3** than **2** with alkoxy side chains confirm the existence of such intermolecular interactions.[6] Meanwhile, these intermolecular electric dipolar interactions induce the dense molecular packing. LC-NR **3** with the higher electric dipole than **1** shows higher melting points; (±)-**3** shows a 17.8 °C higher melting point than (±)-**1** and (2*R*,5*R*)-**3** shows a 24.4 °C higher melting point than (2*S*,5*S*)-**1**.[12] Especially, this type of intermolecular electric dipolar interactions becomes very strong in the racemates; (±)-**3** shows a 21.7 °C higher melting point than (2*R*,5*R*)-**3**. Therefore, in the case of racemates of LC-NRs with positive dielectric anisotropy ($\Delta\varepsilon > 0$) such as (±)-**1** and (±)-**3**, it is expected that the dense molecular packing induced by the intermolecular electric dipolar interactions and by the dimerization of the two enantiomers is likely to be maintained in LC and Iso phases. In such Cr-like molecular packing manner, strong antiferromagnetic interactions between racemic dimers similar to those in Cr phase could occur due to local SOMO-SOMO overlapping[12] and thus the inhomogeneous intermolecular interactions are likely to be suppressed; we conclude that it is the origin of the largest negative magneto-LC effects in LC-NR (±)-**3** with a terminal cyano group.

Conclusions

All-organic LC-NRs **3** and **4** with a terminal cyano group possessing a positive dielectric anisotropy ($\Delta\varepsilon > 0$) showing a

stable N or N* phases exhibited unique magnetic behaviors, which are different from previously reported LC-NRs. Under weak magnetic fields, stronger negative magneto-LC effects occur in the N phase of (±)-**3** than in the N phase of (±)-**1**, whereas positive magneto-LC effects are observed in the N* phase of (2*R*,5*R*)-**3**. Among the bulk N*, SmC*, SmA*, N, and SmC phases of all-organic LC-NRs we have prepared thus far, the N phase of (±)-**3** shows the largest negative magneto-LC effects. The origin of such large negative magneto-LC effects for the N phase of (±)-**3** is interpreted in terms of the generation of antiferromagnetic interactions, which is associated with the formation of the racemic dimers due to the strong intermolecular electric dipolar interactions induced by the terminal cyano group. These experimental results strongly suggest that negative magneto-LC effects could be induced by introducing strong electron-withdrawing substituents such as nitro, trifluoromethyl and pentafluorosulfanyl[40] groups into the molecular terminal position so as to form the racemic dimers. Furthermore, the physical properties of LC-NRs, such as magnetic and optical properties, would become tunable by means of the combination of the positive dielectric anisotropy and homeotropic aligning of these compounds.

Conflicts of interest

There are no conflicts to declare.

Acknowledgements

This work was supported in part by the Japan Science and Technology Agency (JST) “Precursory Research for Embryonic Science and Technology (PRESTO)” for a project of “Molecular technology and creation of new function”, and by Japan Society for the Promotion of Science (JSPS) KAKENHI (Grant number 17H04896). The authors appreciate to Professor Tsuyoshi Kimura and Mr. Hiroki Ueda, Osaka University, for experimental supports including measurements of the magnetic susceptibility, to Professor Rui Tamura, Kyoto University for experimental supports of variable temperature XRD measurements, to Professor Takeshi Naota and Mr. Takatoshi Maeda, Osaka University, for supports of the determination of the X-ray crystal structure, to Dr. Katsuaki Suzuki, Kyoto University, for helpful advices on the synthetic procedures and to JSR Corporation for providing JALS-204. The computations were performed using Research Center for Computational Science, Okazaki, Japan. T.A. is very grateful to the JSPS Research Fellowships for Young Scientists JP16J05585.

Notes and references

‡ CCDC 1570332 contains the supplementary crystallographic data for (±)-**3**. These data can be obtained free of charge via http://www.ccdc.cam.ac.uk/conts/retrieving.html, or from the Cambridge Crystallographic Data Centre, 12 Union Road, Cambridge CB2 1EZ, UK; fax: (+44) 1223-336-033; or e-mail: deposit@ccdc.cam.ac.uk.

1 B. Balasubramanian, B. Das, R. Skomski, W. Y. Zhang and D. J. Sellmyer, *Adv. Mater.*, 2013, **25**, 6090–6093.
2 K. Nakahara, K. Oyaizu and H. Nishide, *Chem. Lett.*, 2011, **40**, 222–227.
3 M. Dvolaitzky, J. Billard and F. Poldy, *Acad. Sci. Ser. C*, 1974, **279**, 533–535.
4 M. Dvolaitzky, J. Billard and F. Poldy, *Tetrahedron*, 1976, **32**, 1835–1838.
5 S. Nakatsuji, M. Mizumoto, H. Ikemoto, H. Akutsu and J. Yamada, *Eur. J. Org. Chem.*, 2002, **2002**, 1912–1918.
6 N. Ikuma, R. Tamura, S. Shimono, N. Kawame, O. Tamada, N. Sakai, J. Yamauchi and Y. Yamamoto, *Angew. Chem. Int. Ed.*, 2004, **43**, 3677–3682.
7 N. Ikuma, R. Tamura, S. Shimono, Y. Uchida, K. Masaki, J. Yamauchi, Y. Aoki and H. Nohira, *Adv. Mater.*, 2006, **18**, 477–480.
8 Y. Uchida, R. Tamura, N. Ikuma, S. Shimono, J. Yamauchi, Y. Aoki and H. Nohira, *Mol. Cryst. Liq. Cryst.*, 2007, **479**, 213/[1251]-221/[1259].
9 R. Tamura, Y. Uchida and N. Ikuma, *J. Mater. Chem.*, 2008, **18**, 2872–2876.
10 Y. Uchida, R. Tamura, N. Ikuma, J. Yamauchi, Y. Aoki and H. Nohira, *Ferroelectrics*, 2008, **365**, 158–169.
11 Y. Uchida, K. Suzuki and R. Tamura, *J. Phys. Chem. B*, 2012, **116**, 9791–9795.
12 K. Suzuki, Y. Uchida, R. Tamura, S. Shimono and J. Yamauchi, *J. Mater. Chem.*, 2012, **22**, 6799–6806.
13 Y. Uchida, K. Suzuki, R. Tamura, Y. Aoki and H. Nohira, *J. Phys. Chem. B*, 2013, **117**, 3054–3060.
14 S. Greve, V. Vill and W. Friedrichsen, *Z. Für Naturforschung B*, 2014, **57**, 677–684.
15 T. Akita, Y. Uchida and N. Nishiyama, *Mol. Cryst. Liq. Cryst.*, 2015, **613**, 174–180.
16 K. Suzuki, Y. Takemoto, S. Takaoka, K. Taguchi, Y. Uchida, D. G. Mazhukin, I. A. Grigor’ev and R. Tamura, *Chem. Commun.*, 2016, **52**, 3935–3938.
17 T. Akita, Y. Uchida, D. Kiyohara, S. Nakagami and N. Nishiyama, *Ferroelectrics*, 2016, **495**, 97–104.
18 T. Akita, Y. Uchida and N. Nishiyama, *Chem. Lett.*, 2016, **45**, 910–912.
19 M. Jasiński, D. Pociecha, H. Monobe, J. Szczytko and P. Kaszyński, *J. Am. Chem. Soc.*, 2014, **136**, 14658–14661.
20 K. Bajzíková, M. Kohout, J. Tarábek, J. Svoboda, V. Novotná, J. Vejpravová, D. Pociecha and E. Gorecka, *J. Mater. Chem. C*, 2016, **4**, 11540–11547.
21 C. V. Yelamaggad, A. S. Achalkumar, D. S. S. Rao, M. Nobusawa, H. Akutsu, J. Yamada and S. Nakatsuji, *J. Mater. Chem.*, 2008, **18**, 3433–3437.
22 S. Castellanos, F. López-Calahorra, E. Brillas, L. Juliá and D. Velasco, *Angew. Chem. Int. Ed.*, 2009, **48**, 6516–6519.
23 P. Ravat, T. Marszalek, W. Pisula, K. Müllen and M. Baumgarten, *J. Am. Chem. Soc.*, 2014, **136**, 12860–12863.
24 M. Jasiński, J. Szczytko, D. Pociecha, H. Monobe and P. Kaszyński, *J. Am. Chem. Soc.*, 2016, **138**, 9421–9424.
25 Y. Uchida, N. Ikuma, R. Tamura, S. Shimono, Y. Noda, J. Yamauchi, Y. Aoki and H. Nohira, *J. Mater. Chem.*, 2008, **18**, 2950–2952.
26 Y. Uchida, K. Suzuki, R. Tamura, N. Ikuma, S. Shimono, Y. Noda and J. Yamauchi, *J. Am. Chem. Soc.*, 2010, **132**, 9746–9752.
27 Y. Uchida, Y. Iwai, T. Akita, T. Mitome, K. Suzuki, R. Tamura and N. Nishiyama, *J. Mater. Chem. B*, 2014, **2**, 4130–4133.

28 K. Suzuki, Y. Uchida, R. Tamura, Y. Noda, N. Ikuma, S. Shimono and J. Yamauchi, *Soft Matter*, 2013, **9**, 4687–4692.
29 S. Talukdar, J.-L. Hsu, T.-C. Chou and J.-M. Fang, *Tetrahedron Lett.*, 2001, **42**, 1103–1105.
30 F. Bloch, *Phys. Rev.*, 1946, **70**, 460–474.
31 I. Dierking, *Textures of Liquid Crystals*, Wiley-VCH, Weinheim, Revised edition., 2003.
32 J. W. Goodby, E. J. Davis, R. J. Mandle and S. J. Cowling, in *Handbook of Liquid Crystals*, Wiley-VCH Verlag GmbH & Co. KGaA, 2014.
33 B. Bleaney and K. D. Bowers, *Proc. R. Soc. Lond. Math. Phys. Eng. Sci.*, 1952, **214**, 451–465.
34 M. J. Frisch, G. W. Trucks, H. B. Schlegel, G. E. Scuseria, M. A. Robb, J. R. Cheeseman, G. Scalmani, V. Barone, B. Mennucci, G. A. Petersson, H. Nakatsuji, M. Caricato, X. Li, H. P. Hratchian, A. F. Izmaylov, J. Bloino, G. Zheng, J. L. Sonnenberg, M. Hada, M. Ehara, K. Toyota, R. Fukuda, J. Hasegawa, M. Ishida, T. Nakajima, Y. Honda, O. Kitao, H. Nakai, T. Vreven, J. A. Montgomery, Jr., J. E. Peralta, F. Ogliaro, M. Bearpark, J. J. Heyd, E. Brothers, K. N. Kudin, V. N. Staroverov, R. Kobayashi, J. Normand, K. Raghavachari, A. Rendell, J. C. Burant, S. S. Iyengar, J. Tomasi, M. Cossi, N. Rega, J. M. Millam, M. Klene, J. E. Knox, J. B. Cross, V. Bakken, C. Adamo, J. Jaramillo, R. Gomperts, R. E. Stratmann, O. Yazyev, A. J. Austin, R. Cammi, C. Pomelli, J. W. Ochterski, R. L. Martin, K. Morokuma, V. G. Zakrzewski, G. A. Voth, P. Salvador, J. J. Dannenberg, S. Dapprich, A. D. Daniels, O. Farkas, J. B. Foresman, J. V. Ortiz, J. Cioslowski and D. J. Fox, *Gaussian 09, Revision D.01*, Gaussian, Inc., Wallingford CT, 2009.
35 S. Yamanaka, T. Kawakami, H. Nagao and K. Yamaguchi, *Chem. Phys. Lett.*, 1994, **231**, 25–33.
36 R. Improta, K. N. Kudin, G. E. Scuseria and V. Barone, *J. Am. Chem. Soc.*, 2002, **124**, 113–120.
37 H. J. Müller and W. Haase, *J. Phys.*, 1983, **44**, 1209–1213.
38 B. L. Bales, M. Peric and M. T. Lamy-Freund, *J. Magn. Reson.*, 1998, **132**, 279–286.
39 K. Yamaguchi, M. Okumura, J. Maki, T. Noro, H. Namimoto, M. Nakano, T. Fueno and K. Nakasuji, *Chem. Phys. Lett.*, 1992, **190**, 353–360.
40 P. R. Savoie and J. T. Welch, *Chem. Rev.*, 2015, **115**, 1130–1190.

